Contents lists available at ScienceDirect

Acta Materialia

Full length article

Measurement and simulation of pressure drop across replicated porous aluminium in the Darcy-Forchheimer regime

A.J. Otaru [a], H.P. Morvan [a], A.R. Kennedy [b, *]

[a] Gas Turbine & Transmissions Research Centre, Faculty of Engineering, University of Nottingham, NG7 2RD, UK
[b] Engineering Department, Lancaster University, Bailrigg, Lancaster, LA1 4YW, UK

ABSTRACT

Experimental measurements of the pressure drop across porous metals have been compared with computational fluid dynamics simulations, for the first time, for structures typified by large pores with small interconnecting "windows". Structural information for the porous structures was obtained from X-ray computed tomography and a robust methodology for developing a representative volume element is described. The modelling approach used was able to reliably predict the pressure drop behaviour within the Forchheimer regime. The methodology was extended to simulate flow through geometrically-adapted, "semi-virtual" pore structures and this approach could prove to be an invaluable tool in the design of porous metal components for applications involving fluid flow.

© 2018 Acta Materialia Inc. Published by Elsevier Ltd. All rights reserved.

Background

Open cell porous metals are commonly used as structures that interact with a fluid in processes such as heat exchange and storage, filtration and catalysis. Pivotal to the performance of these structures is the resistance to fluid flow that is provided by the porous body, usually described by the pressure drop per unit length developed across the structure as a function of the flow rate (or velocity) of the fluid through it. Knowing or predicting and then controlling the pressure-drop is key to optimising the performance of these structures and to designing new structures with enhanced or novel attributes.

Fluid flow through porous materials is normally associated with energy being dissipated as a result of the interaction between the two phases. For a very slow fluid flow, a viscous-drag energy dissipation mechanism dominates and the pressure-drop-airflow velocity relationship is described by the Hazen-Darcy equation [1,2];

$$\frac{\Delta P}{L} = \frac{\mu}{K} \, v \tag{1}$$

where ΔP is the pressure difference across the length of the porous

material in the flow direction (Pa), L is the sample thickness in the same direction (m), K is the permeability (m^2), μ is the fluid viscosity (Pa s) and v is the Darcian velocity (m s^{-1}), the volumetric flow rate divided by the cross sectional flow area. For flow behaviour obeying this case, the fluid is said to be flowing in the Darcy regime [2,3].

As the fluid velocity increases, the Hazen-Darcy equation fails to describe the pressure-drop behaviour [2]. A quadratic term, referred to as the Forchheimer or the form drag term, is added to equation (1) in order to capture the effect of the force exerted by any solid surface on the flowing fluid and its resultant effect on the pressure drop. This yields equation (2), which is known as the Hazen-Dupuit-Darcy or Forchheimer equation:

$$\frac{\Delta P}{L} = \frac{\mu}{K} \, v + \, C\rho v^2 \tag{2}$$

where ρ is the fluid density (kg m^{-3}) and C is the form drag coefficient (m^{-1}) which is related to the structure of the permeable medium [3]. For typical fluid velocities and pore-size ranges used in engineering flow systems, the Forchheimer equation most accurately describes the fluid flow [4].

Since the K and C terms in the Forchheimer equation are affected by facets of the structure of the porous metal, for example porosity, cell size and the morphology of the pores and the pore-network, altering the porous metal structure has the potential to greatly influence the pressure drop across it. It is vital to adopt a

---

* Corresponding author.
  E-mail address: a.kennedy3@lancaster.ac.uk (A.R. Kennedy).

processing route that can manufacture high quality porous metal structures with reproducible structures, but additionally, these processes must enable some adaptability to tailor the geometrical features to enable the flow behaviour through the porous material to be altered to suit the service requirements.

The infiltration of liquid metal into a bed of sacrificial particles (often termed porogens or space fillers) offers a convenient and reproducible method for the manufacture of porous metals [5–8] with the potential to vary the porosity and pore size independently, thereby giving a good level of control over the structure and hence the fluid flow behaviour [5,6,9]. Using this method a "preform" is made from the porogen either from loose or tapped beads, or using subsequent compaction, with or without sintering steps. Infiltration with a molten metal is then affected by applying either a positive pressure to the metal or a vacuum to the porogen bed. The pore structure in the porous metal is thus a negative of the morphology and spatial arrangement of the porogen.

Fig. 1 shows the typical structure of porous metals made by replication of packed beds of near-spherical NaCl beads [10]. The most important structural feature of porous metals made in this way is the presence of small windows that connect the pores. The number of particle-particle contacts (the coordination number for packing) primarily dictates the number of windows connecting the pores. The highlighted pore in Fig. 1 has at least 7 windows to neighbouring pores. The size of these windows is governed by the extent to which infiltrating liquid can penetrate within the region between contacting (or very close) particles and this is a function of the infiltration pressure (the capillary radius) the bead geometry and the packing behaviour.

Studies combining computational fluid dynamics (CFD) simulations and experimental measurements of flow through very open porous metals, often made by replication of reticulated polymer foams, are reasonably common (an excellent overview is given in Ref. [2]). Approaches that use X-ray computed tomography to capture the solid and fluid domains have been successful in predicting the pressure drop to within 5% of the experimentally observed behaviour [12,13]. Such simulations have not been extended to porous metals made by replication of packed beds of beads. Simple analytical permeability models for laminar (Darcy) flow have been developed [4,14] and, supported by modelling [11], they show the flow behaviour to be dominated by the small windows between the pores (as marked in Fig. 1) which create a "bottleneck" to flow through the structure. The model in Ref. [4] was extended to flow in the Forchheimer regime in Ref. [15] where it was shown that both the K and C terms are more strongly influenced by the size of the windows that connect the pores than the pore diameter.

This paper aims to develop a robust simulation methodology for predicting the pressure drop across porous metals with bottleneck-type structures and to test it against experimental measurements. It is hoped that the findings will contribute to the development of methodologies for structural optimisation of these porous structures.

1. Experimental procedure

1.1. Specimen manufacture

Porous Al samples were made by a replication process (similar to that described in Ref. [10]) using salt beads (Hydrosoft) as a sacrificial porogen and a vacuum casting method. Castings were made by pouring 2–2.5 mm salt beads into a 35 mm diameter flanged stainless steel mould with a porous base. The flanged mould was pre-heated to 600 °C and part-inserted into a vacuum chamber and when molten 99.5% purity Al was poured onto the top of the bed of beads, a pressure differential was applied to drive infiltration of the molten metal therein. The pressure differential was measured, and varied by controlling an outlet valve fixed to the vacuum chamber, such that the pressure differential varied between approximately 0.9–0.25 bar in four increments. Cast samples were machined into 25 mm diameter cylinders, 34.5 mm long, where after the salt beads were removed by dissolution in warm water.

1.2. Specimen characterisation

X − ray CT imaging was performed on each of the different porous Al samples using an Xradia 500 instrument, with a voxel dimension of 26 μm. The Scan IP module within Simpleware™, a 3D image processing, analysis and model generation software package, was used to create a 3D representation from the 2D CT slices. Image processing methods, such as thresholding and creating masks or outlines to follow the boundaries between the 2 phases, were found to have a significant effect on the accuracy of the representation of the porous structure and were thus optimised to ensure that characteristic pore features were as accurately reproduced as was possible and that there was less than a $\pm0.25\%$ deviation between the nominal porosity of the thresholded image and that for the real foam structure. In addition to the porosity, the mean pore and window size were also determined from the 3D CT volume using a watershed segmentation method and by computing a mean minimum area of circles along the centrelines adjoining two pores
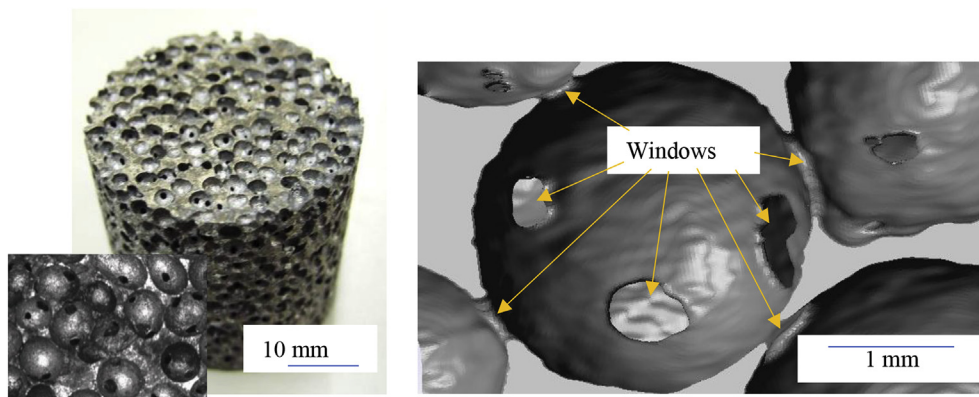

Fig. 1. Optical micrographs, left for a porous sample made by vacuum casting using near-spherical NaCl beads [10] and right, an X-ray CT image showing the typical pore connectivity [11].

respectively. Comparisons were made with measurements from optical microscope images using image analysis software, Image J.

1.3. Experimental measurement of pressure drop

The experimental setup used to measure the pressure drop across porous samples at a defined air flow rate, is shown in Fig. 2. The experimental arrangement and measurement methods are similar to those reported in Refs. [13,16,17]. In brief, the apparatus consists of a compressed air supply with filter and pressure regulator, a flow control valve and flow rate meter, a flow straightener and a sample holder for the porous Al samples. Samples with a diameter of 25 mm, 34.5 mm long, were placed in the tube and were wrapped with polytetrafluoroethylene (PTFE) tape to prevent bypass of the air.

The pressure either side of the sample was measured using GEMS pressure transducers (0–2.5 bar range for the inlet), the data from which were logged by a PC for 3 min at each flow rate, ensuring a steady state had been achieved before the flow rate was increased. The flow rate was varied to achieve superficial velocities in the range of approximately $0.6-2.4 \, \mathrm{m \, s^{-1}}$. The pressure drop ($\Delta P$) across the foam length was calculated ensuring compressibility effects were considered [2] using equation (3), where P_i and P_0 are the inlet and outlet absolute pressures respectively (P_0 was always ambient pressure) and P_R is a reference pressure (ambient). The accuracy, reproducibility and mean standard deviation (typically < 1.5%) for the measurements are discussed in Ref. [16]. Samples were measured at least 3 times and a mean pressure drop was recorded at each velocity.

$$\Delta P = \frac{P_i^2 - P_o^2}{2P_R} \quad (3)$$

1.4. CFD simulation of permeability

Computational fluid dynamics (CFD) simulation of air flow through these porous structures was performed by solving the steady − state compressible Navier − Stokes equation (suitable only for laminar flow) on a meshed fluid domain within a representative volume element (RVE), using the Single-Phase flow module in COMSOL Multiphysics 5.0™. The size of the RVE, which was extracted from the centre of the scanned samples, was determined by shrinking a much larger volume until the porosity differed by no more than 0.25% from the initial (bulk) value, typically giving an x, y, z, RVE dimension between $8 \times 8 \times 8$ and $8 \times 8 \times 10$ mm.

The boundary conditions and methodologies used to extract pressure data are similar to those reported in Ref. [13]. In brief, a zero outlet pressure was applied to suppress backflow and no slip boundary conditions were applied to the walls. The unidirectional pressure drop across the porous structure was measured by taking the difference between the surface average values of the computed inlet and the outlet (zero) pressures for a series of simulations at different fixed values of flow velocity, between 0.6 and $2.36 \, \mathrm{m \, s^{-1}}$.

Preliminary simulations were performed to determine a workable balance between mesh scale, convergence time and accuracy. A linear tetrahedral mesh was used, varying the minimum cell size seeded at the fluid-solid interface (from 1.5x to 5x the resolution of the image), keeping the mesh growth rate constant (at 1.3x) and setting the maximum cell size, occurring in the centres of the pores, to 6.75x the minimum value. Fig. 3 plots the effect of increasing the mesh density on the ratio of the pressure drop compared to that for the solution for the finest mesh, which was set by the maximum number of cells (circa 6M) that the computational power available could solve. The "optimum" was selected as having a minimum cell size of 2.7x the image resolution (26 μm), creating a mesh with 2.7M cells. A less than a 0.2% difference (increase) in pressure drop was observed compared with the maximum mesh density, with less than 1/10th of the runtime. Two-dimensional images for the mesh structures, for the same connected pores, are also shown in Fig. 3 for the coarsest, finest and "optimum" cases.

2. Results and discussion

2.1. Structural characterisation

Fig. 4 shows typical porous Al structures, with examples shown for the highest and lowest pressure differentials. They show near-spherical pores and multiple connections between these pores in
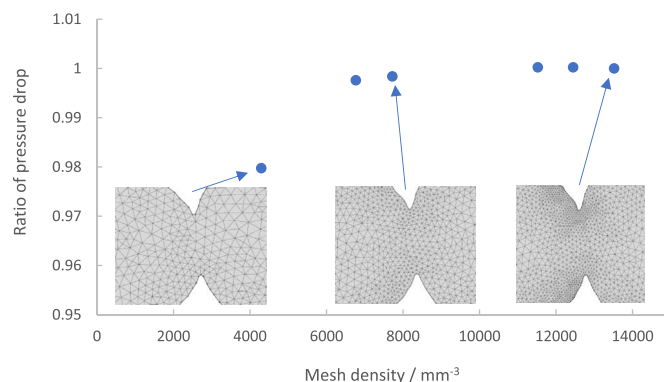
Fig. 3. The effect of increasing mesh density on the ratio of the pressure drop compared to that for the solution for the finest mesh. Mesh structures for the coarsest, finest and "optimum" cases are shown.
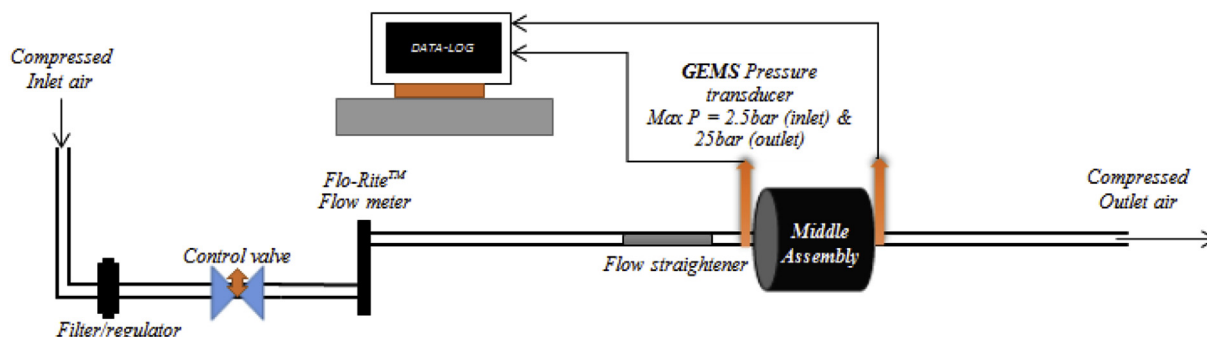
Fig. 2. Schematic representation of the apparatus for pressure drop measurement.
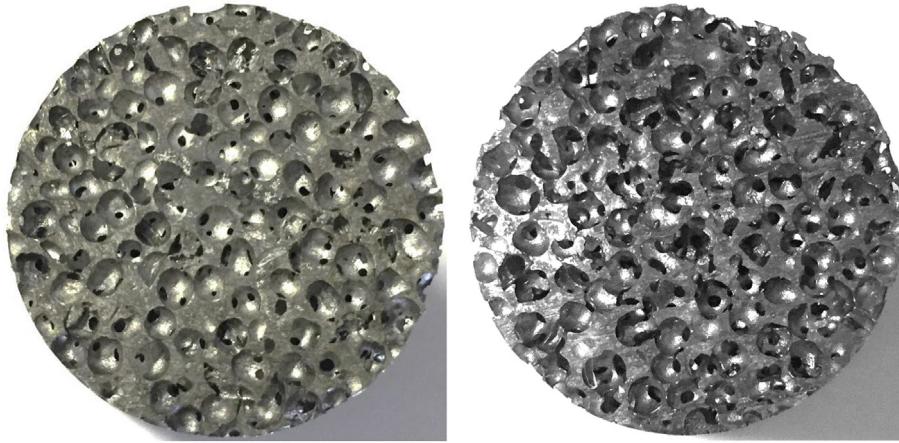
Fig. 4. Optical microscope images of porous Al foam structures made at (left) the highest and (right) the lowest pressure differential (samples are 25 mm in diameter).

the form of smaller, rounded "windows". It was apparent that not only does the size of these windows increase as the pressure differential decreases, but the number per pore also increases. Previous studies by these authors [10,11] have shown that although the number of windows per cell is broadly dependent upon the coordination number for packing of the bead structure, typically 6–7 for monosized spheres, higher for irregularly-shaped beads such as those used in this study, this can increase significantly as the pressure differential is decreased, as liquid is less able to fill small spaces at the contact points between beads.

Fig. 5 shows an optical microscope image for a porous Al sample and a typical 2D CT slice extracted from it. Fig. 6 shows how the image processing methodology was optimised to ensure the outline of the porosity was accurately followed, in particular making sure that the contact regions between the particles, which have a smaller radius of curvature for higher pressure differentials, were accurately represented. This figure also shows the corresponding 3D structures, highlighting the different morphologies at the extremes of the pressure differentials investigated.

Table 1 presents structural data for the porous metals produced, showing the key parameters of porosity, mean pore size and mean connectivity (window) size measured from 3D CT volumes (CFD). The measurements of pore diameter and connectivity taken from micrographs (EXP), also shown in this table, confirm the veracity of those measured from the CT images. The porosities determined experimentally from the dimensions and mass, also agree closely with those determined from the CT images.

Structural measurements bear out the trends expected. The bead size dictates the pore size, smaller connections between pores are observed as the casting pressure differential increases and although the porosity is primarily dictated by the packing behaviour of the beads, it also influenced by the infiltration pressure, with higher pressure differentials leading to more complete filling of the pore network and to lower levels of porosity. Fig. 7 shows the relationship between the pressure differential and the ratio of the mean window size to pore size.

2.2. Experimental measurement of flow

Fig. 8 shows the pressure drop characteristics for the range of different porous structures produced, where an order of magnitude difference in the pressure drop per unit length is observed between structures with the highest and lowest porosity, at the maximum flow rate. The pressure drop behaviour is split into three groups; the highest pressure drop is observed for the sample with the lowest porosity and smallest windows, similar intermediate behaviour is observed for samples with similar, intermediate window sizes and the lowest pressure drops are observed for the sample with highest porosity and largest windows. The similarity in pressure drop behaviour for P3 and P2 (which have similar window sizes but differ in porosity by 2.5%) indicates the relatively small effect of changes in porosity. It should be noted that the scatter in pressure drop values from repeat measurements is smaller than the symbol used to mark the data points.
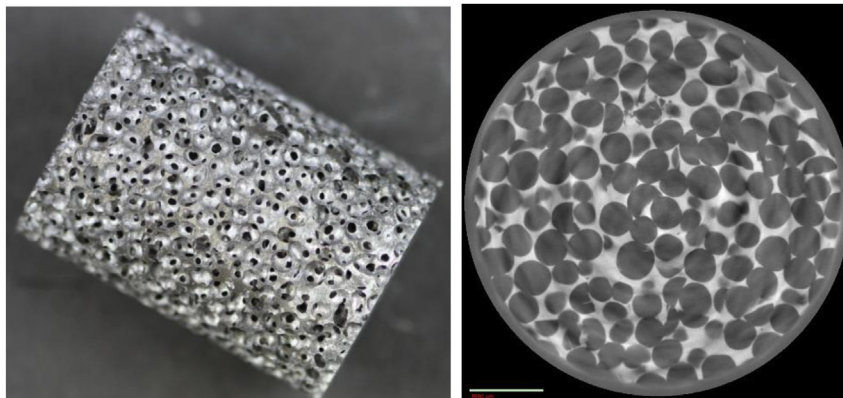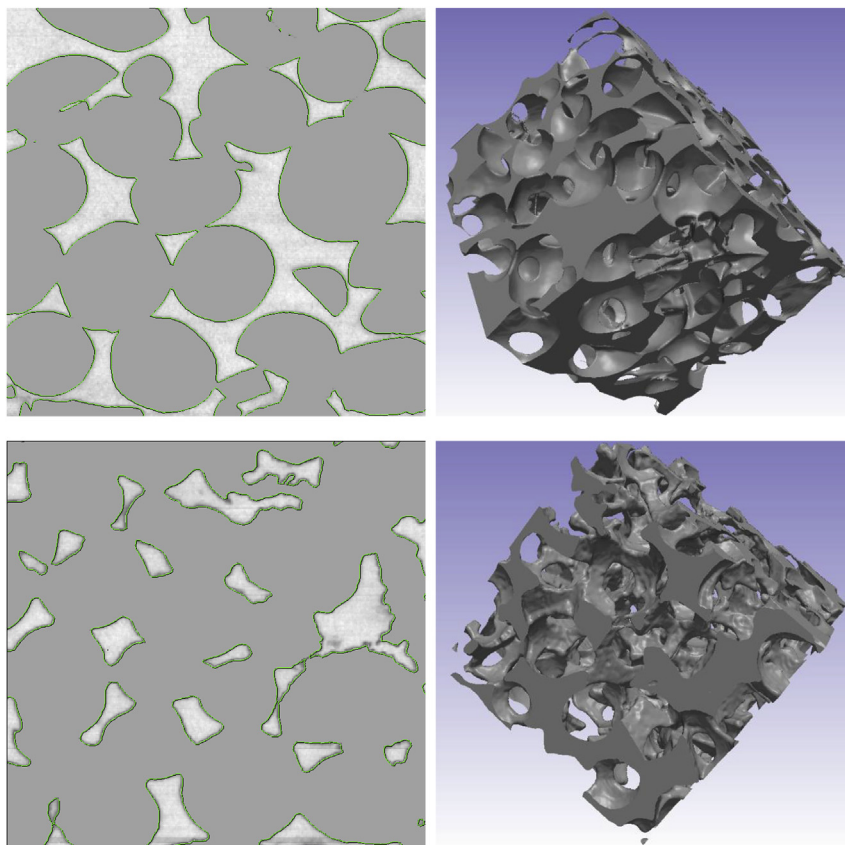

Fig. 5. 3D optical and corresponding 2D X-ray CT images of a porous Al structure (samples are 25 mm in diameter).

Fig. 6. Left, 2D model contours and right, metal domains for porous Al made at the highest (top) and lowest (bottom) pressure differentials (3D constructions are 8 × 8 × 8 mm).

Table 1
Structural parameters for porous Al structures measured from CT images (CFD) and directly from the samples (EXP).

	Pressure difference (bar)	Porosity (%)	Mean pore size, (mm)	Mean connectivity (mm)
P1 CFD	–	70.5	2.23 ± 0.17	0.65 ± 0.02
P1 EXP	0.90 ± 0.02	70.6	2.21 ± 0.15	0.64 ± 0.02
P2 CFD	–	72.6	2.22 ± 0.17	0.72 ± 0.02
P2 EXP	0.60 ± 0.02	72.6	2.23 ± 0.12	0.73 ± 0.02
P3 CFD	–	75.2	2.27 ± 0.15	0.74 ± 0.02
P3 EXP	0.45 ± 0.01	75.1	2.22 ± 0.16	0.75 ± 0.02
P4 CFD	–	78.4	2.23 ± 0.24	0.90 ± 0.02
P4 EXP	0.25 ± 0.01	78.2	2.24 ± 0.25	0.92 ± 0.03

By plotting the reduced pressure drop, the pressure drop per unit length divided by the superficial velocity, against the superficial velocity, the relevant flow regimes can be identified to ensure that the modelling approach is apt [18]. Fig. 8 presents such a plot and shows that for all the samples, the dependence is linear, with very close fit, indicating that the flow is within the Forchheimer regime across the entire range of velocities explored.

The Reynolds number for flow (calculated using the pore diameter as the length scale) ranges from roughly 90 to 350 over the interval of flow velocities explored. This would suggest a transition in the flow behaviour should be observed at close to $1 \, \text{m s}^{-1}$ (Re = 150), from the Forchheimer to the post Forchheimer regime, and a further transition to turbulent flow for velocities above $2 \, \text{m s}^{-1}$ (Re = 300) [19]. The clear absence of these transitions highlights the inadequacy of using the pore diameter to define the length scale when determining the Reynolds number for these types of porous structure.

2.3. Simulation of flow

Fig. 9 shows the simulated flow behaviour (flow is from top to bottom) through samples with the highest and lowest porosity (P1 and P4) at a superficial inlet velocity of $1 \, \text{m s}^{-1}$. Bottleneck flow is apparent through preferential "channels" controlled by the availability and alignment of the windows in each pore. The intensity of this constrictive effect is shown by the regions of stagnant flow and of high velocity that correspond to the scale, and which are also indicated by the velocity vectors. It can be seen that fluid exiting the bottleneck regions in the P1 structure (with the smallest windows) does so with a velocity that is approaching 15x that for the superficial velocity and which is more than 3x times higher than that for corresponding flow in the P4 structure (with the largest windows).

For the P1 sample, made at the highest pressure difference, the number of windows in each pore is the smallest [10,11] and this reduces the likelihood of more than one "exit" window being aligned in the flow direction, encouraging the flow to become more
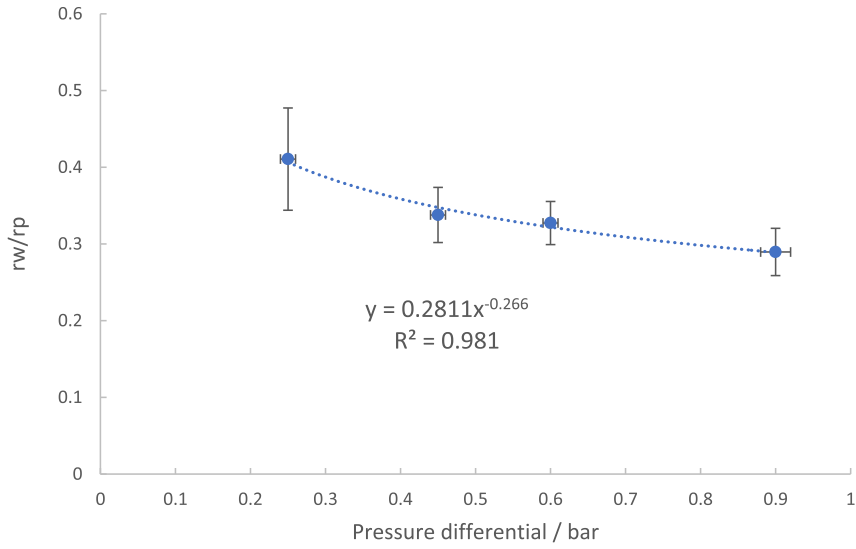
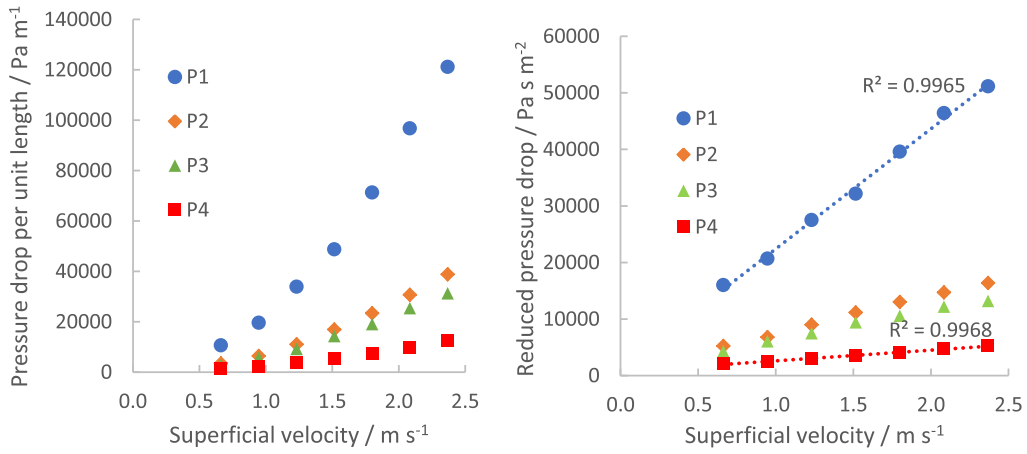**Fig. 7.** Relationship between pressure differential and ratio of window to pore size for the cast samples.

Fig. 8. Plots of (left) pressure drop per unit length and (right) reduced pressure drop against superficial flow velocity.
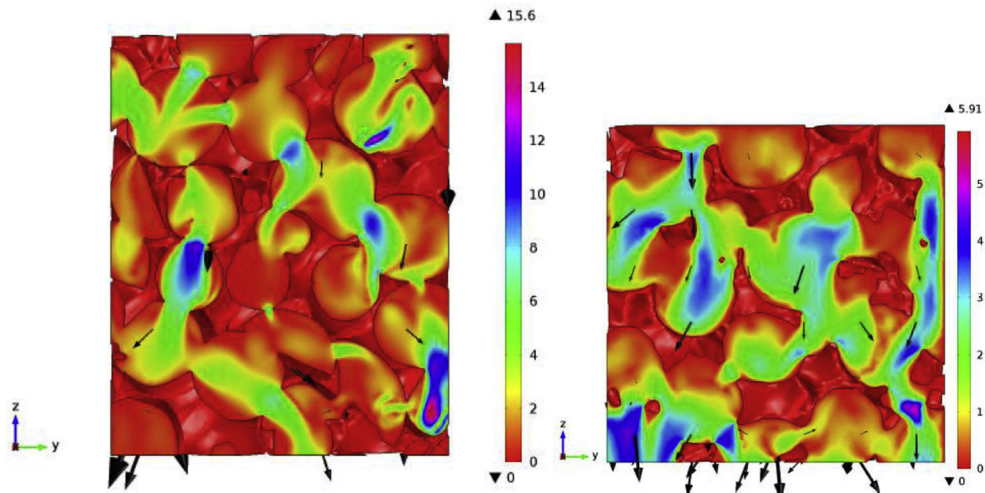

Fig. 9. 2D sections of the velocity distribution for flow through porous samples P1 (left) and P4 (right) for a superficial velocity of 1m s^{-1} (RVE for P1 is 8 × 8 × 10 mm, for P4 it is 8 × 8 × 8 mm).

tortuous. In contrast, the P4 sample, with the highest porosity and most numerous and largest windows, creates the least "diversion" to the incoming airflow and exhibits the fewest regions where flow stagnates.

2.4. Comparing simulations and experimental measurements

Fig. 10 compares the pressure drop per unit length vs velocity curves for experimental measurements and modelling. Good agreement is observed for all samples, with average RMS fits to the experimental data of 99, 105, 95 and 102%, as the porosity increases respectively, without consistent over or under prediction of the pressure drop. These deviations are within established limits for "accurate" modelling of more open porous metal structures [12].

The permeability and form drag coefficients, as defined in the Forchheimer equation, were obtained by fitting a second order polynomial (with a regression coefficient higher than 0.999 in all cases) to experimental data and data from simulations, and are given in Table 2, where good agreement between the two sets is observed. From this, the individual contributions to the pressure drop per unit length from the two terms in the Forchheimer equation can be determined, and it is observed (as in Ref. [21]) that the contribution from the form drag term increases with velocity, in this instance over the range of 64–99%. Thus for these bottleneck-type structures and the range of flow velocities investigated, form drag dominates the pressure drop behaviour.

When compared with the analytical model in Ref. [15], data fit more closely to predictions for C than for K (as was observed in Ref. [15]). The inertial term, C and the form factor, $C\sqrt{K}$, tend to be more closely predicted (within typically 20%) for samples with numerous and large openings between pores, where flow more closely resembles the unperturbed flow pattern assumed in the model. The model isn't, however, able to accurately predict the pressure drop behaviour in the same way that the more time-consuming simulations can, especially for sample P1 which experiences tortuous flow, for which K and C are predicted to be 40–50% of the experimentally determined values.

2.5. Modelling considerations

It is rarely possible to have similar RVE and experimental test sample sizes owing to the extremely high mesh count and computational power that would be required. Whilst the process for determining an RVE will minimise variations in porosity between the modelled volume and the sample, differences in pore morphology may arise for non-homogeneous structures, such as
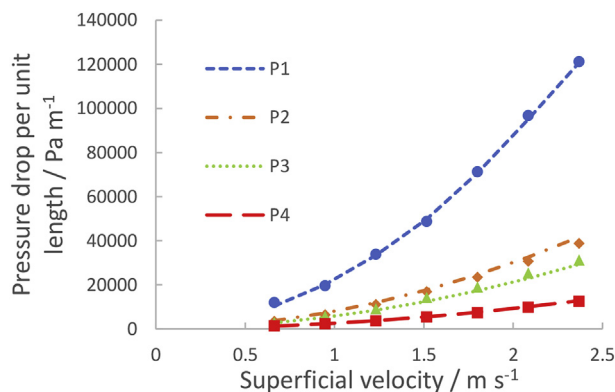
Table 2
Forchheimer equation terms for flow simulations (CFD) and experimental measurements (EXP).

	Permeability (K)/$10^{-09}\mathrm{m}^2$	Form drag (C) m^{-1}
P1 CFD	13.5	17466
P1 EXP	13.2 ± 0.15	17283 ± 225
P2 CFD	17.1	5802
P2 EXP	17.0 ± 0.23	5417 ± 84
P3 CFD	18.0	3986
P3 EXP	19.3 ± 0.41	4491 ± 63
P4 CFD	33.4	1700
P4 EXP	31.2 ± 0.53	1636 ± 21

those examined in this study. Accurate modelling is dependent upon accurate representation of the porous structure by both sampling a "typical" volume and ensuring both the CT data capture and the image processing stages preserve the accuracy of the pore and window geometry. Despite the local inhomogeneities within these structures, it was found that pressure drop measurements for simulations on RVE's taken from different regions within the same sample differed by less than 2% if the porosities differed by no more than 0.5%.
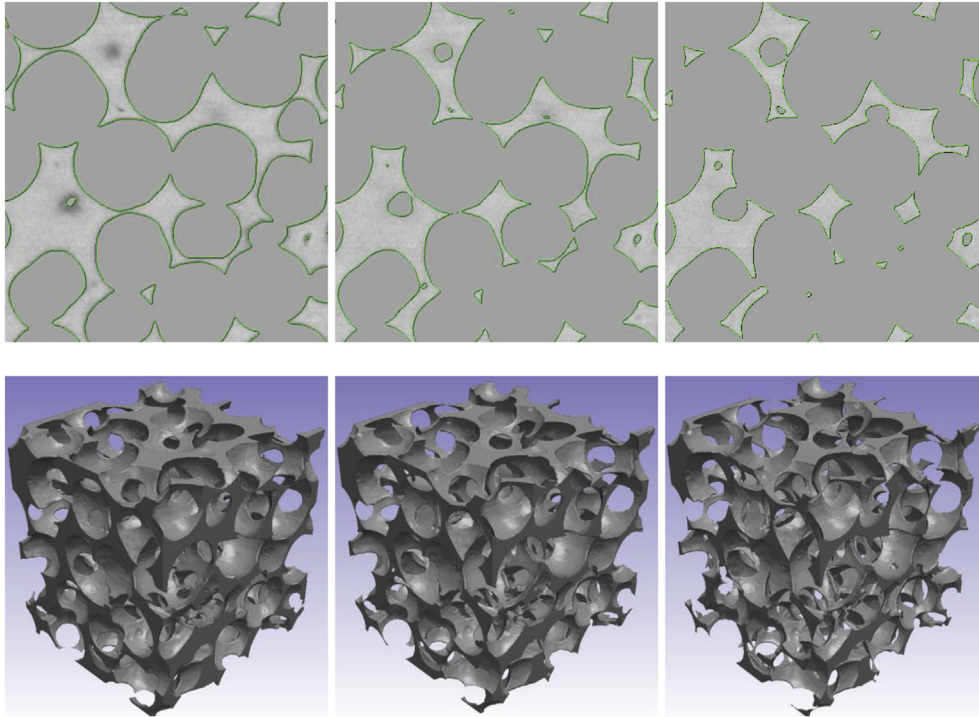
Discrepancies between simulations and experimental measurements may arise from using an RVE size based on the structure, rather than the flow geometry [13]. Structure-derived RVE's are generally smaller in length than the "critical" sample length required for developing flow behaviour that is length independent (found by both experimentation and simulation for more open and more porous metal structures to be some 20–50 pore diameters in thickness [13,16,17,20]). One study [17] reported pressure drop increases of up to 25% for samples that were smaller than the critical length.

In this study, changes in the RVE length (in the flow direction) from 6 mm to 15 mm produced very little variation in the pressure drop determined from simulations. Despite small differences in porosity ($\pm 0.3\%$) produced by "sectioning" the non-uniform structure, the pressure drop at the highest flow velocity remained within 97% of that for the largest RVE. The lack of observable length effect is worth remarking. It is thought that in the materials studied here, channelling of the flow through the much more restricted passages in the structure encourages a more rapid transition from flow in the pipe to distorted flow within the porous structure than occurs in more open structures such as those reported in Refs. [2,13,16,17,20].

2.6. Simulation of semi-virtual structures

CT images from real structures were modified to create semi-virtual 3D volumes. Adding or subtracting pixels (dilation or erosion) to the solid field is similar in principle to applying higher or lower pressure differences during casting. This approach could, therefore, aid the understanding of the effects of changes in structure on the pressure drop behaviour, without the need to cast samples.

Fig. 11 presents 2D views from the same CT section for images for the P3 structure and for semi-virtual samples with 1 (P31) and 2 (P32) pixels removed from the metal field; equivalent to creating a sample at 2 successively lower pressure differentials. From the 3D images, the opening of the windows connecting the pores and the increase in porosity are clear. It should be noted that over-erosion can lead to isolated struts and this should be avoided. Table 3 quantifies the structural changes corresponding to the images and presents the K and C values for the pressure drop per unit length-superficial velocity dependence. A substantial increase in K and decrease in C is apparent, consistent with those affected by

Fig. 10. Graph of measured (symbols) and modelled (dashed lines) pressure drops per unit length against superficial velocity.

Fig. 11. 2D CT images (top) and 3D volumes (bottom) for sample P3 (left) and after erosion of 1 (centre, P31) and 2 (right, P32) pixels from the solid field (3D constructions are 8 × 8 × 8 mm).

Table 3
Comparison of structural parameters for "real" and semi-virtual structures derived from sample P3 (shown in Fig. 11) after erosion of the solid field.

|	Porosity/%	Dw (mm)	Dp (mm)	Permeability (K)/10^{-09}m^2	Form drag (C) m^{-1}
CFD P3	75.2	2.27 ± 0.15	0.74 ± 0.02	18.0	3986
V31	80.9	2.36 ± 0.20	0.92 ± 0.02	35.4	2668
V32	85.9	2.48 ± 0.21	1.16 ± 0.02	58.9	1085

structural changes as a result of reductions in pressure difference, as reported in Table 2. It should be noted that by increasing the resolution of the CT images, a finer level of adjustment to the structural parameters could be made.

Dimensionless analysis enables the effect of multiple changes in porosity, pore size and window size that are affected by the erosion process to be rationalised. Fig. 12 plots the permeability and form drag in dimensionless form (shown in equations (4) and (5)) against the ratio of window to pore size for real and virtual structures made by multiple erosions of samples P1-P4.

$$K^* = \frac{K}{\varnothing\, r_p^2} \tag{4}$$

$$C^* = C\, r_p\, \varnothing^2 \tag{5}$$

The figures show that data for real and semi-virtual structures fall on broadly the same curves and follow the same form, and are of similar magnitude, to those from experimental data in Ref. [15]. Thus, the adaptation of real porous structures in this way appears to
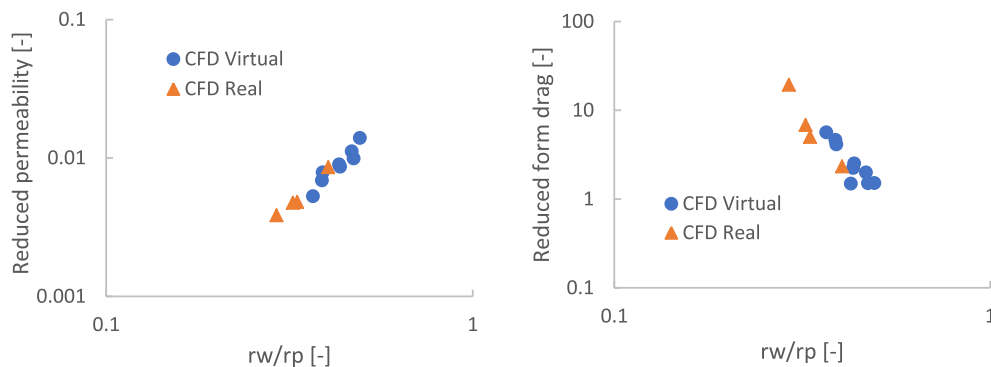
Fig. 12. Plots of the reduced permeability and form drag against the ratio of window to pore diameter for real and semi-virtual structures.

be a valid method to determine the effect of changes in structural morphology on the flow behaviour through these types of porous structures.

Such a limited number of simulations could then be wide-reaching in their ability to aid the design of porous structures of this type. For example, after selecting a porogen size and porosity (packing fraction), as well as target values for the pressure drop, equation (2) can be used, with a representative flow velocity, to determine K and C (although for higher velocities C dominates and K could be neglected in a first iteration). With a value for C^* calculated, plots in Fig. 12 give the ratio of window to pore size required to achieve it (and K could be determined if needed and the process iterated). Plots of the form presented in Fig. 7 can then be used to define the pressure differential required to achieve the target window size.

3. Summary

The modelling approach used here has been shown to reliably predict the pressure drop behaviour within the Forchheimer regime in replicated foam structures with bottleneck-type pore structures. Achieving accurate predictions (correlations between experiment and simulation within <5%) requires accurate representation of the porous structure. Geometrical adaptations of real porous structure can be used to create structures that bear resemblance to real ones. This enables an appreciation of the effect of changes in porosity and window size on the pressure drop, without the need for sample production. Such an approach could be invaluable in the design of porous components with bottleneck-type structures.

References

[1] E. Baril, A. Mostafid, L.-P. Lefebvre, M. Medraj, Experimental demonstration of entrance/exit effects on the permeability measurements of porous materials, Adv. Eng. Mater. 10 (2008) 889–894.

[2] N. Dukhan, Metal Foams: Fundamentals and Applications, Destech Publications Incorporated, Lancaster, PA, 2013.

[3] D. Ingham, I. Pop, Transport Phenomena in Porous Media, first ed., vol. 1, Elsevier Science Ltd, Oxford, UK, 1998.

[4] J.-F. Despois, A. Mortensen, Permeability of open-pore microcellular materials, Acta Mater. 53 (2005) 1381–1388.

[5] R. Goodall, J.F. Despois, A. Marmottant, L. Salvo, A. Mortensen, The effect of preform processing on replicated aluminium foam structure and mechanical properties, Scripta Mater. 54 (2006) 2069–2073.

[6] R. Goodall, A. Marmottant, L. Salvo, A. Mortensen, Spherical pore replicated microcellular aluminium: processing and influence on properties, Mater. Sci. Eng. A465 (2007) 124–135.

[7] A. Jinnapat, A.R. Kennedy, The manufacture and characterisation of aluminium foams made by investment casting using dissolvable spherical sodium chloride bead preforms, Metals 1 (2011) 49–64.

[8] A. Jinnapat, A.R. Kennedy, Characterisation and mechanical testing of open cell Al foams manufactured by molten metal infiltration of porous salt bead preforms: effect of bead size, Metals 2 (2012) 122–135.

[9] J.F. Despois, A. Marmottant, L. Salvo, A. Mortensen, Influence of the infiltration pressure on the structure and properties of replicated aluminium foams, Mater. Sci. Eng. 462 (2007) 68–75.

[10] P. Langston, A.R. Kennedy, Discrete element modelling of the packing of spheres and its application to the structure of porous metals made by infiltration of packed beds of NaCl beads, Powder Technol. 268 (2014) 210–218.

[11] A.J. Otaru, A.R. Kennedy, The permeability of virtual macroporous structures generated by sphere packing models: comparison with analytical models, Scripta Mater. 124 (2016) 30–33.

[12] A. Diani, K.K. Bodla, L. Rossetto, S.V. Garimella, Numerical investigation of pressure drop and heat transfer through reconstructed metal foams and comparison against experiments, Int. J. Heat Mass Tran. 88 (2015) 508–515.

[13] T.P. de Carvalho, H.P. Morvan, D.M. Hagreaves, H. Oun, A.R. Kennedy, Pore-scale numerical investigation of pressure drop behaviour across open-cell metal foams, Transport Porous Media 117 (2017) 311–336.

[14] E.L. Furman, A.B. Finkelstein, M.L. Cherny, Permeability of aluminium foams produced by replication casting, Metals 3 (2013) 49–57.

[15] L. Weber, D. Ingram, S. Guardia, A. Athanasiou-Ioannou, A. Mortensen, Fluid flow through replicated microcellular materials in the Darcy-Forchheimer regime, Acta Mater. 126 (2017) 280–293.

[16] H. Oun, A.R. Kennedy, Experimental investigation of pressure-drop characteristics across multi-layer porous metal structures, J. Porous Mater. 21 (2014) 1133–1141.

[17] H. Oun, A.R. Kennedy, Tailoring the pressure-drop in multi-layered open-cell porous inconel structures, J. Porous Mater. 22 (2015) 1627–1633.

[18] K. Boomsma, D. Poulikakos, The effects of compression and pore size variations on the liquid flow characteristics of metal foams, ASME Journal of Fluids Engineering 124 (2002) 263–272.

[19] M.H. Pedras, M.J.S. de Lemos, Macroscopic turbulence modeling for incompressible flow through undeformable porous media, Int. J. Heat Mass Tran. 44 (2001) 1081–1093.

[20] N. Dukhan, P. Patel, Equivalent particle diameter and length scale for pressure drop in porous metals, Exp. Therm. Fluid Sci. 32 (2008) 1059–1067.

[21] S. De Schampheleire, K. De Kerpel, B. Ameel, P. De Jaeger, O. Bagci, M. De Paepe, A discussion on the interpretation of the Darcy equation in case of open-cell metal foam based on numerical simulations, Materials 9 (2016) 409.